Journal of Scientific Research and Development (2025) Vol. 24 (1) 111-123

JSRD
Journal of Scientific
Research & Development

A bi-annual journal published by the Faculty of Science, University of Lagos, Nigeria
http://jsrd.unilag.edu.ng/index.php/jsrd

Numerical simulation of a lead-free double perovskite heterostructure device with different charge transport layers

Muteeu A. Olopade^{a,b*} and David Aderibigbe^{b}

^{a} Department of Physics, Faculty of Physical and Earth Sciences, University of Lagos, Nigeria

^{b}Department of Physics, Fourah Bay College, University of Sierra Leone, Sierra Leone

* Corresponding author: muteeu.olopade@usl.edu.sl

(Received 23 May 2025/Revised 17 August 2025/Accepted 22 August 2025)

Abstract

Perovskite solar cells can convert more than 25% of insolation which is comparable to silicon solar cells. However, they are yet to be deployed on a large scale because they rely on poisonous lead and unstable. Researchers are now investigating lead-free double perovskites, which have good optoelectronic properties and are safe for the environment. Lanthanum nickel manganese oxide (LNMO) stands out due to its adjustable band gap and chemical stablity. This makes it an excellent contender for long-lasting photovoltaic uses. In this work, we employ SCAPS-1D device simulations to systematically optimize the photovoltaic performance of LNMO (Lanthanum Nickel Manganese Oxide) based heterostructure cells through band-gap engineering of the absorber layer from 1.0 eV up to 2.2 eV, screening of six electron-transport layers (TiO□, PCBM, C□□, IGZO, WS□, CeO□) against twelve hole-transport layers (PEDOT:PSS, CuSCN, Spiro-OMeTAD, etc.) to identify the best charge-extraction interfaces, and thickness variation studies for the optimal ETL/HTL pairing. Our results reveal that WS□ combined with PEDOT: PSS yielded a power-conversion efficiency (PCE) of 23.7 %, outperforming conventional TiO□-based architectures. Further optimization of the LNMO absorber thickness shows a maximum PCE of 27.18 % at 1 450 nm, with corresponding open-circuit voltage (Voc) of 1.261 V, short-circuit current density (Jsc) of 27.62 mA cm□², and fill factor (FF) of 78.03 %. These findings deliver concrete design guidelines with optimal band-gap window (1.50–1.625 eV), preferred ETL/HTL combination (WS□/PEDOT: PSS), and absorber thickness (~1.45 µm) for realizing high-efficiency, stable, lead-free Perovskite Solar Cells.

KEY WORDS: Perovskites, solar cells, transport layers, optimisation

---

Introduction

Perovskite solar cells (PSCs) have attracted significant research interest due to their impressive power conversion efficiencies (PCEs) reaching over 25% (Kojima et al., 2009; NREL, 2023; Liu et al., 2023), competitive with silicon solar cells, alongside their low-cost and low-temperature fabrication processes (Kumar et al., 2020). However, the prevalent use of lead in perovskite absorbers raises serious environmental and health concerns, and the inherent instability of these materials under operational conditions limits their commercial viability (Kumar et al., 2020; Babayigit et al., 2016, Gharibzadeh et al., 2021). These challenges have propelled the search for lead-free alternatives, with lead-free double perovskites emerging as promising candidates owing to their non-toxic nature and enhanced chemical stability (Sheikh et al., 2017; Hossain et al., 2022; McClure et al., 2016; Greul et al., 2017: Raoui et al., 2021; Li et al., 2024).

Lead-free double perovskites of the form A□B'B"O□, where A represents rare-earth cations and B', B" are transition metals, have shown potential for photovoltaic applications. Materials such as La□NiMnO□ (LNMO), Eu□NiMnO□ (ENMO), and Dy□NiMnO□ (DNMO) possess favorable band gaps (~1.0–1.6 eV) and high dielectric constants, which help reduce charge recombination and improve carrier diffusion length, essential for efficient solar energy conversion (Sheikh et al., 2017; Lan et al., 2016; Sariful Sheikh et al., 2017). Experimental studies have demonstrated moderate PCEs for these oxides, but their performance is still limited compared to lead-based counterparts (Sheikh et al., 2017; Zhang et al., 2019). For instance, LNMO-based devices have reported efficiencies below 10%, largely constrained by suboptimal band gaps, high defect densities, and challenges in achieving effective charge transport (Sheikh et al., 2017).

Optimizing the absorber's band gap is crucial for maximizing solar cell efficiency. Theoretical models and experimental data indicate that an optimal band gap for single-junction solar cells lies between 1.4 and 1.7 eV, where the trade-off between photon absorption and voltage output is balanced (Zhang et al., 2019; Shockley and Queisser, 1961; Jiang et al., 2023). Recent simulation work using SCAPS-1D has validated this range for LNMO, ENMO, and DNMO, reporting peak PCEs of approximately 9.7%, 9.4%, and 9.0%, respectively, at tuned band gaps between 1.5 and 1.625 eV (Sheikh et al., 2017, Li et al., 2024). These results underscore the importance of band gap engineering for lead-free double perovskite absorbers.

Beyond the absorber material, the choice and optimization of charge transport layers (CTLs)—electron transport layers (ETLs) and hole transport layers (HTLs) are essential to enhance charge extraction and reduce recombination losses. Traditional PSC designs frequently use TiO□ as ETL and PEDOT: PSS or Spiro-OMeTAD as HTL; however, these materials exhibit drawbacks such as poor conductivity, cost, and instability (Bencherif et al., 2022). Recent studies employing a broader range of ETLs (e.g., PCBM, ZnO, SnO□, WS□, CeO□) and HTLs (e.g., CuSCN, CBTS, CuI) in combination with lead-free double perovskite absorbers have demonstrated significant improvements in device performance. For example, CBTS as HTL paired with various ETLs achieved PCEs exceeding 20% in Cs□BiAgI□-based devices, indicating that interface engineering and CTL selection critically impact overall solar cell efficiency (Kung et al., 2020; Bencherif et al., 2022; Et-taya et al., 2020; Chakraborty et al., 2019).

Despite the promising chemical stability and non-toxicity of lead-free double perovskites, their wider and less-tunable band gaps, coupled with limited exploration of diverse ETL/HTL combinations, restrict light harvesting and efficient charge transport. This results in suboptimal PCEs and hinders their competitiveness with lead-based PSCs (Kumar et al., 2020; Sheikh et al., 2017). Moreover, many studies focus on a narrow range of materials and fixed absorber compositions, lacking comprehensive analysis of how band gap tuning synergizes with transport layer optimization to enhance device performance (Kumar et al., 2020; Raoui et al., 2021; Jiang et al., 2023).

The current literature reveals a gap in integrated approaches that combine absorber band gap engineering with systematic screening of a wide spectrum of ETL and HTL materials to identify optimal device architectures. Few investigations couple first-principles calculations (e.g., Density Functional Theory) with device-level simulations (SCAPS-1D) to holistically optimize both material properties and device performance in lead-free PSCs (Kung et al., 2020). Addressing this gap is critical to designing high-efficiency, stable, and commercially viable lead-free PSCs capable of surpassing present efficiency limits.

Methodology

Device structure and design

The solar cell heterostructure device was modeled as a planar layered structure using the SCAPS-1D simulation software (version 3.3.11) developed by ELIS-Ghent University. The device consisted of the following layers:

Front contact: Fluorine-doped tin oxide (FTO), Electron transport layer (ETL): WS□, Absorber layer: Lead-free double perovskite LaNMO (Lanthanum Nickel Manganese Oxide), Hole transport layer (HTL): PEDOT: PSS, Back contact: Gold (Au) as shown in fig. 1 below.

This configuration was chosen to explore the combined effects of absorber band gap tuning and ETL/HTL material selection on photovoltaic performance.

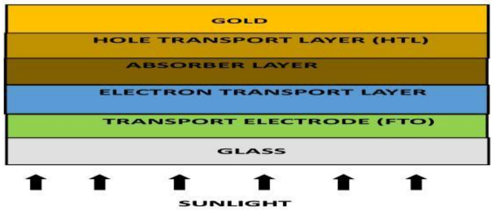

Fig. 1: Schematics of the different layers of the proposed solar cell

Parameterization of materials and simulation conditions

Material parameters including band gap (Eg), electron affinity (χ), dielectric permittivity (ε), thickness, doping concentrations (Na, Nd), carrier mobilities (μn, μp), and defect densities were assigned to each layer based on a comprehensive literature review and experimental reports on similar materials.

Illumination was simulated using the standard AM1.5G solar spectrum, and all baseline simulations were carried out at a temperature of 300 K, with additional sweeps between 280 K and 330 K to assess thermal effects. Voltage sweeps were performed to extract current–voltage (J–V) characteristics and compute the key metrics—open-circuit voltage (Voc), short-circuit current density (Jsc), fill factor (FF), and power conversion efficiency (PCE). Tables 1, 2 and 3 depict the parameters used in the simulation processes.

Parameter sweeps and optimization

To identify optimal device parameters, we conducted systematic parameter sweeps in which the LNMO absorber band gap was incrementally adjusted from its initial value (~1.05 eV) up to the optimized range (~1.50 eV). We screened six electron-transport layers—including WS_2, TiO_2, and PCBM—and twelve hole-transport layers—such as PEDOT: PSS, CuSCN, and Spiro-OMeTAD—to determine the combinations that yielded the best performance. In addition, the thicknesses of the absorber, ETL, and HTL layers were varied to achieve the ideal balance between light absorption and charge extraction. Finally, defect densities and doping concentrations were tuned to minimize recombination losses and optimize the built-in potential.

Table 1: Input optimization parameters of the FTO, ETL, and absorber layer of the study

Parameters	FTO (BACK CONTACT)	TiO_2	PCBM	C_{60}	IGZO	WS_2	CeO_2	LNMO (ABSORBER)
Thickness (nm)	500	300	50	50	30	100	100	350
Band gap (eV)	3.50	3.20	2.00	1.70	3.05	1.80	3.50	1.50
Electron affinity (eV)	4.00	4.00	3.90	3.90	4.16	3.95	4.60	3.520
Dielectric permittivity	9.0	9.0	3.9	4.2	10.0	13.5	9.0	3.500
CB effective DOS (cm^{-3})	2.2×10^{18}	2.2×10^{18}	2.5×10^{21}	8.0×10^{19}	5.0×10^{18}	1.0×10^{18}	1.0×10^{20}	1.0×10^{18}
VB effective DOS (cm^{-3})	1.8×10^{19}	1.8×10^{19}	2.5×10^{21}	8.0×10^{19}	5.0×10^{18}	2.4×10^{19}	2.0×10^{21}	1.0×10^{18}
Electron mobility ($cm^2/V\cdot s$)	20	20	0.20	0.08	15	100	100	22.0
Hole mobility ($cm^2/V\cdot s$)	10	10	0.20	0.0035	0.10	100	25	22.0
N_a (cm^{-3})	0	0	0	0	0	0	0	0
N_D (cm^{-3})	1.0×10^{21}	1.0×10^{21}	2.93×10^{17}	1.0×10^{17}	1.0×10^{17}	1.0×10^{18}	1.0×10^{21}	7.0×10^{16}
Defect density (cm^{-3})	1.0×10^{15}	1.0×10^{15}	1.0×10^{15}	1.0×10^{15}	1.0×10^{15}	1.0×10^{15}	1.0×10^{15}	1.0×10^{15}

Table 2: Input optimization parameters HTL the study

Parameters	Cu_2O	CuSCN	$CuSbS_2$	P3HT	PEDOT:PSS	Spiro-OMeTAD	NiO	CuI	CuO	V_2O_5	CFTS	CBTS
Thickness (nm)	50	50	50	50	50	200	100	100	50	100	100	100
Band gap (eV)	2.2	3.6	1.58	1.7	1.6	3.0	3.8	3.1	1.51	2.2	1.3	1.9
Electron Affinity (eV)	3.4	1.7	4.2	3.5	3.4	2.2	1.46	2.1	4.07	4.0	3.3	3.6
Dielectric permittivity	7.5	10	14.6	3	3	3	10.7	6.5	18.1	10	9	5.4
CB effective DOS (cm^{-3})	2×10^{19}	2.2×10^{19}	2×10^{18}	2×10^{21}	2.2×10^{18}	2.2×10^{18}	2.8×10^{19}	2.8×10^{19}	2.2×10^{19}	9.2×10^{17}	2.2×10^{18}	2.2×10^{18}
VB effective DOS (cm^{-3})	1×10^{19}	1.8×10^{18}	1×10^{18}	2×10^{21}	1.8×10^{19}	1.8×10^{19}	1×10^{19}	1×10^{19}	5.5×10^{20}	5×10^{18}	1.8×10^{19}	1.8×10^{19}
Electron mobility ($cm^2/V\cdot s$)	200	100	49	1.8×10^{-3}	4.5×10^{-2}	2.1×10^{-3}	12	100	100	3.2×10^{2}	21.98	30
Hole mobility ($cm^2/V\cdot s$)	8600	25	49	1.86×10^{-2}	4.5×10^{-2}	2.16×10^{-3}	2.8	43.9	0.1	4.0×10^{1}	21.98	10
N_A (cm^{-3})	1×10^{18}	1×10^{18}	1×10^{18}	1×10^{18}	1×10^{18}	1×10^{18}	1×10^{18}	1×10^{18}	1×10^{18}	1×10^{18}	1×10^{18}	1×10^{18}
N_D (cm^{-3})	0	0	0	0	0	0	0	0	0	0	0	0
Defect density (cm^{-3})	1×10^{15}	1×10^{15}	1×10^{15}	1×10^{15}	1×10^{15}	1×10^{15}	1×10^{15}	1×10^{15}	1×10^{15}	1×10^{15}	1×10^{15}	1×10^{15}

Table 3. Input parameters of interface defect layer

Interface	Defect Type	Capture Cross section: electron/holes	Energetic distribution	Reference for defect energy level	Total Density
ETL/Layer	Neutral	1×10^{-17} 1×10^{-18}	Single	Above the VB maximum	1×10^{10}
Layer/HTL	Neutral	1×10^{-18} 1×10^{-19}	Single	Above the VB maximum	1×10^{10}

Data analysis

Simulation outputs were analyzed to compare photovoltaic performance across different parameter sets. Trends in open□circuit voltage (Voc), short□circuit current density (Jsc), fill factor (FF), and power conversion efficiency (PCE) were plotted and examined to identify optimal band□gap windows and material pairings. Emphasis was placed on interface quality, given its critical role in charge extraction efficiency and the mitigation of recombination losses.

Results and discussion

To clearly present the performance of different device configurations, we begin this section with a comparative analysis of electron transport layers (ETLs) paired with multiple hole transport layers (HTLs). The figures below summarize the simulated photovoltaic parameters—open-circuit voltage (Voc), short-circuit current density (Jsc), fill factor (FF), and power conversion efficiency (PCE)—for each ETL/HTL combination using an LNMO absorber.

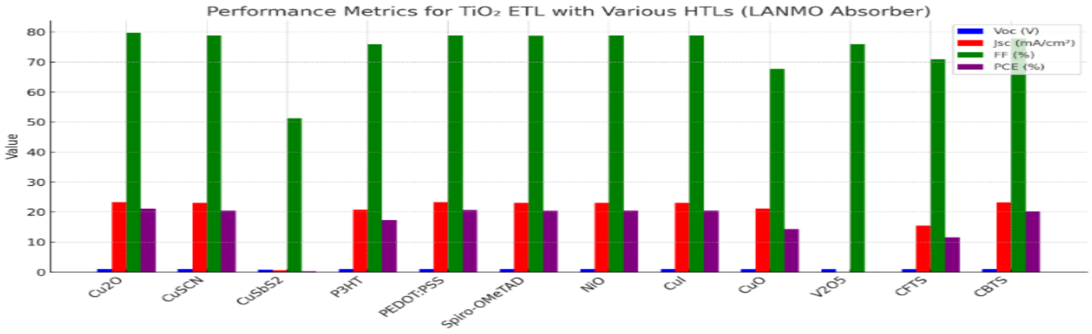

Figure 2. *Performance Metrics (Voc, Jsc, FF, PCE) for TiO_2 ETL with Various HTLs Using a LANMO Absorber*

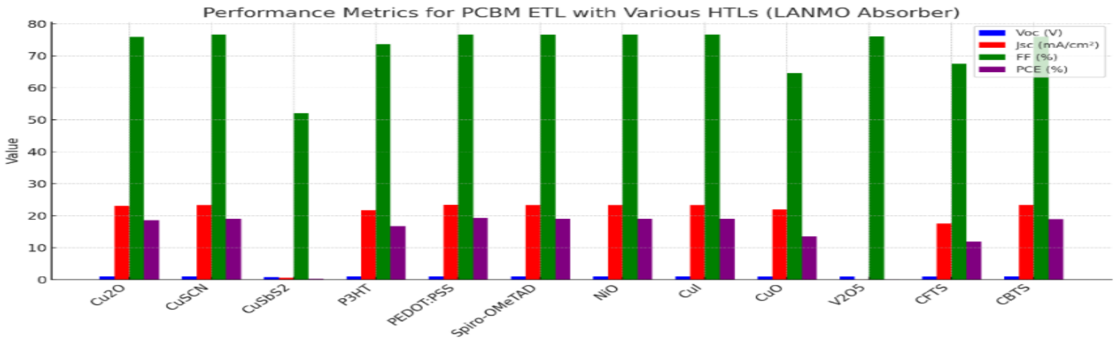

Figure 3. *Performance Metrics (Voc, Jsc, FF, PCE) for PCBM ETL with Various HTLs Using a LANMO Absorber*

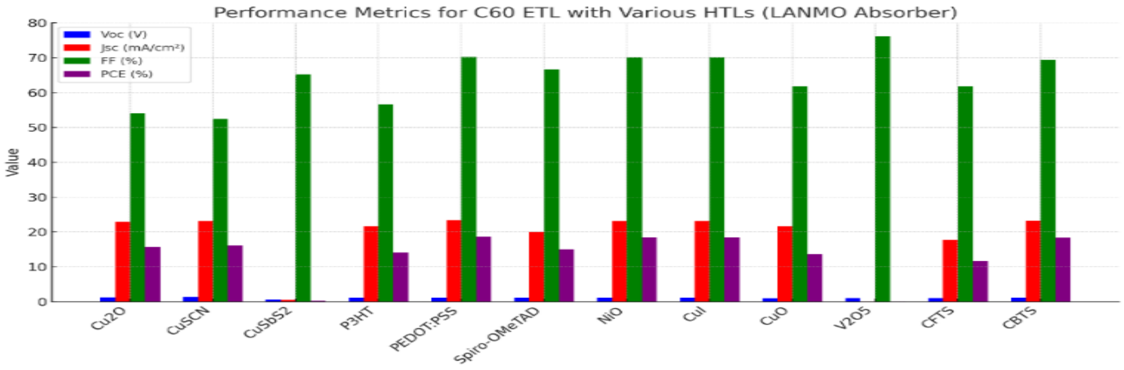

Figure 4. *Performance Metrics (Voc, Jsc, FF, PCE) for C60 ETL with Various HTLs Using a LANMO Absorber*

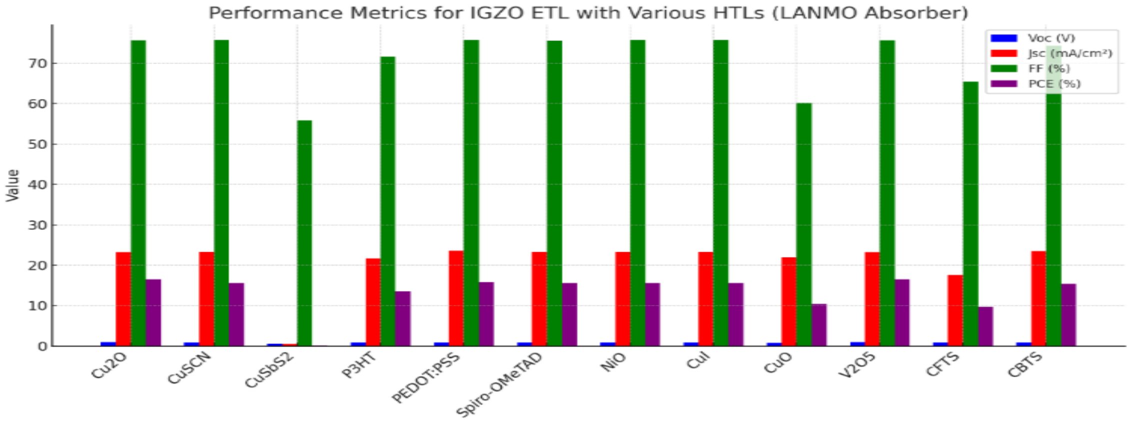

Figure 5. *Performance Metrics (Voc, Jsc, FF, PCE) for IGZO ETL with Various HTLs Using a LANMO Absorber*

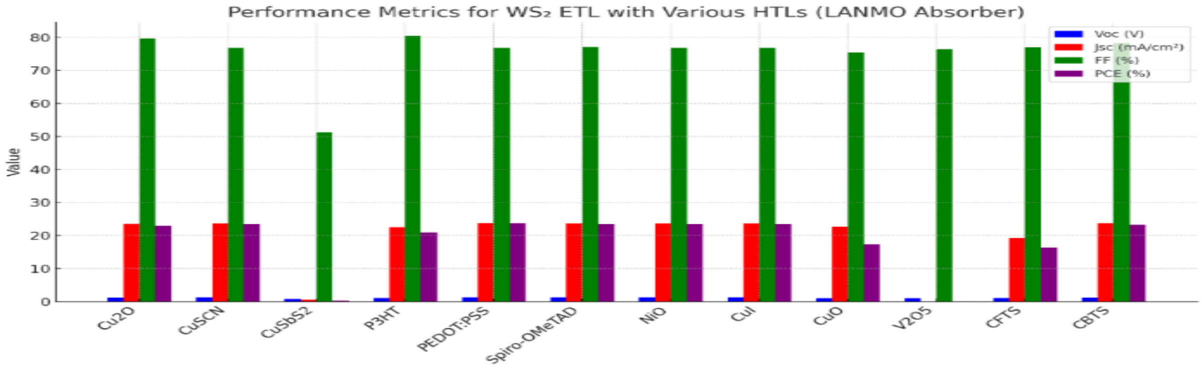

Figure 6. *Performance Metrics (Voc, Jsc, FF, PCE) for WS_2 ETL with Various HTLs Using a LANMO Absorber*

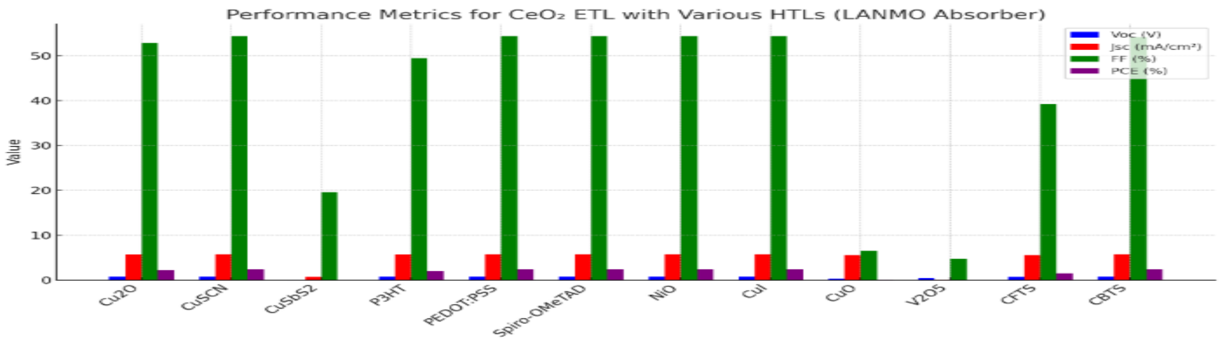

Figure 7. *Performance Metrics (Voc, Jsc, FF, PCE) for CeO_2 ETL with Various HTLs Using a LANMO Absorber*

The performance charts reveal (Figure 6) that among the six electron- transport layers tested with the LNMO absorber, WS_2 consistently delivers the highest power conversion efficiencies, reaching 23.7 % when paired with PEDOT:PSS and 23.5 % with CuSCN. This superior performance stems from WS_2's excellent electron extraction, which drives high short- circuit currents (around 23.9 mA/cm²) and robust fill factors (approximately 76.8 %). TiO_2 follows closely behind (Figure 2): its devices achieve peak efficiencies of about 21.2 % with both Cu_2O and CuSCN as the hole- transport layer, owing to a comparatively high open- circuit voltage (≈1.08 V) and fill factors exceeding 83 %.

In contrast, organic fullerene- based ETLs like PCBM and C60 (Figure 3 and Figure 4) produce moderate efficiencies in the 18–19 % range when used with PEDOT:PSS, reflecting adequate but inferior electron mobility relative to WS_2 and TiO. IGZO- based devices (Figure 5) show somewhat lower performance, peaking at about 15.6 % efficiency with PEDOT:PSS, largely because their open- circuit voltage is limited to around 0.88 V despite reasonable fill factors near 75 %. CeO_2 stands out as the poorest performer (Figure 7): its devices suffer very low short- circuit currents (below 6 mA/cm²) and open- circuit voltages (~0.76 V), resulting in efficiencies under 2.4 %, which indicates that CeO_2 is not a viable ETL for LNMO absorbers.

Across all ETLs, PEDOT:PSS emerges as the most consistently effective hole- transport layer, delivering high fill factors and facilitating efficient hole extraction. CuSCN also performs strongly, particularly in combination with WS_2 and TiO_2. While Spiro- OMeTAD yields respectable results, it never surpasses the performance achieved with PEDOT:PSS or CuSCN in these simulations.

Examining the key metrics in detail, the highest open- circuit voltages are observed with TiO_2 (~1.08 V) and WS_2 (~1.29 V), whereas CeO_2 lags behind at ~0.76 V. Short- circuit currents peak under WS_2 (~23.9 mA/cm²) and plateau for fullerene ETLs (~23.3 mA/cm²), but they collapse for CeO_2 devices. Fill factors are maximized with TiO_2 (>83 %) and WS_2 (~80 %), moderate with PCBM and C60 (~76 %), and lowest with CeO_2 (~54 %).

In summary, the optimal configuration for LNMO- based solar cells in this study combines an inorganic ETL—specifically WS_2—with a PEDOT:PSS or CuSCN hole- transport layer to achieve efficiencies above 23 %. This combination leverages high voltages and currents along with strong fill factors, whereas CeO_2- based devices exhibit prohibitively poor performance across all metrics.

Variaton of the thickness of the workable etl and htl to optimise efficiency

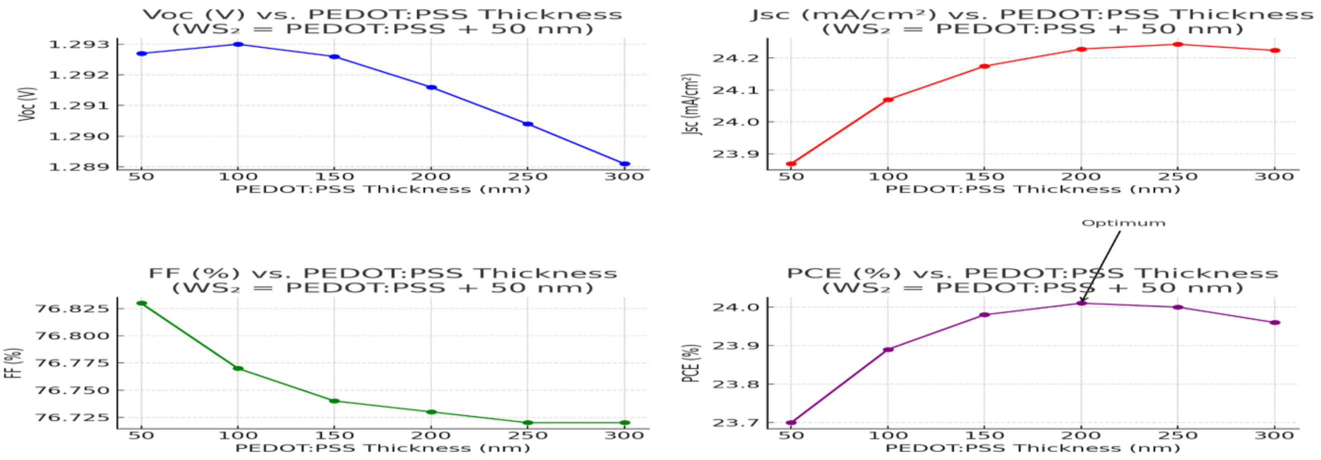

Figure 8. *Effect of PEDOT:PSS and* WS_2 *Thickness Variation on Device Performance Metrics (Voc, Jsc, FF, PCE)*

When the PEDOT:PSS layer is varied from 50 to 300 nm (with the WS_2 ETL held 50 nm thicker), the open-circuit voltage (Voc) peaks at about 1.293 V around 100 nm PEDOT: PSS before gradually declining to 1.289 V at 300 nm. In contrast, (Figure 8) the short-circuit current density (Jsc) steadily increases from 23.87 mA/cm² at 50 nm to a maximum of 24.24 mA/cm² at 250 nm, then flattens. The fill factor (FF) experiences a slight drop—from 76.83 % down to 76.72 %—as the bilayer thickens, reflecting increased series resistance. The combined effect of these trends produces a peak power conversion efficiency (PCE) of 24.01 % at a PEDOT:PSS thickness of 200 nm (and WS_2 at 250 nm). Beyond this point, efficiency gains plateau and begin to reverse, indicating that the optimal thickness combination for maximizing device performance is 200 nm of PEDOT:PSS with 250 nm of WS_2 .

Increase the thickness of the absorber layer

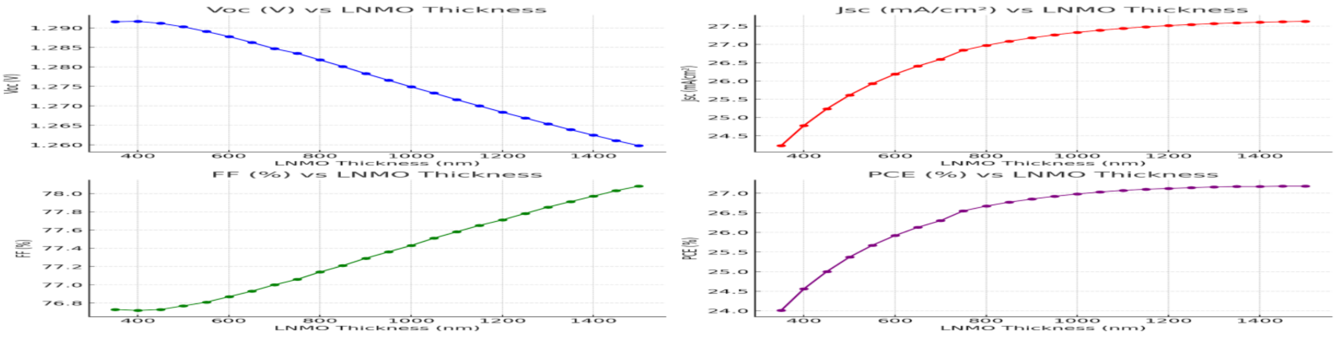

Figure 9. *Effect of LNMO absorber thickness on key device metrics* (Voc, Jsc, FF, PCE)

Maintaining the PEDOT: PSS layer at 200 nm and the WS_2 ETL at 250 nm—the optimal combination identified earlier—we varied the LNMO absorber thickness from 350 nm up to 1500 nm. As shown in Figure 9, increasing LNMO thickness initially boosts light harvesting and fill factor, driving Jsc from ~24.2 to ~27.6 mA/cm^2 and FF from ~76.7 % to ~78.1 %. However, thicker films also introduce more recombination losses, causing Voc to decline slightly from ~1.292 V down to ~1.260 V. When these competing trends are combined, the device's power conversion efficiency rises from 24.0 % at 350 nm to a maximum of 27.18 % at 1450 nm, beyond which it plateaus. This plateau is consistent with the physical limitation imposed by the carrier diffusion length of the absorber material: once the thickness exceeds the diffusion length, photogenerated carriers recombine before contributing to photocurrent, leading to diminishing returns despite increased optical absorption. From an experimental standpoint, this indicates that absorber layers thicker than the diffusion length would not yield practical efficiency gains, and optimal fabrication should therefore balance absorption depth with carrier collection efficiency.

Conclusion

Through comprehensive SCAPS-1D simulations, we have demonstrated that combining absorber band-gap tuning, broad transport-layer screening, and precise layer-thickness optimization can propel lead-free double perovskite solar cells to efficiencies rivalling and even surpassing many lead-based counterparts. Specifically, WS□ as the ETL paired with PEDOT:PSS as the HTL emerges as the most effective interface, delivering over 23 % PCE, while fine-tuning the LNMO absorber thickness to approximately 1 450 nm further boosts performance to 27.18 %. These results underscore the critical interplay between material properties and device architecture. Future work should focus on experimental validation of these optimized configurations, assessment of long-term thermal and environmental stability, and exploration of scalable fabrication methods to translate this simulation-driven design blueprint into commercial-grade, lead-free perovskite photovoltaics

References

Ahmed, I. (2025). Lead-free perovskites for solar cell applications. *Chemical Communications*. https://doi.org/10.1039/d4cc06835a

Babayigit, A., Ethirajan, A., Müller, M., and Conings, B. (2016). Toxicity of organometal halide perovskite solar cells. *Nature Materials, 15*(3),247–251. https://doi.org/10.1038/nmat4572

Bencherif, H., Emetere, M. E., Mohammed, M. K. A., and Pandey, R. (2022). Electron transport and hole transport materials in perovskite solar cells. *RSC Advances, 12*, 12345–12379. https://doi.org/10.1039/D2RA00000A

Chakraborty, K., Kumar, A., Raj, A., Anshul, A., and Kumar, M. (2019). SCAPS simulation of TiO□/Cu□ZnSnSe□ heterostructures for solar cells. *Solar Energy, 180*, 48–56.

https://doi.org/10.1016/j.solener.2019.01.013

Et-taya, L., Hamidat, A., Bouarissa, N., and Zeb, A. (2020). Optimization of Cu□ZnSn(SxSe□□$_{x}$)□ solar cells via SCAPS simulation. *Solar Energy, 201*,827–834. https://doi.org/10.1016/j.solener.2020.03.089

Gharibzadeh, S., Abdollahi Nejand, B., Jakoby, M., Abzieher, T., Hauschild, D., Moghadamzadeh, S., and Paetzold, U. W. (2021). Record open-circuit voltage in perovskite solar cells via atomic layer deposition interface engineering. *Advanced Energy Materials, 11*(20),2100504. https://doi.org/10.1002/aenm.202100504

Greul, E., Petrus, M. L., Binek, A., Docampo, P., and Bein, T. (2017). Highly stable, phase-pure Cs□AgBiBr□ double perovskite thin films for optoelectronic applications. *Journal of Materials Chemistry A, 5*(40), 19972–19981. https://doi.org/10.1039/C7TA05114K

Hasan, M. M. (2025). Next-generation lead-free solar cells with MASnBr□ and ZnSnN□ dual-absorber configuration. *Frontiers in Materials*. https://doi.org/10.3389/fmats.2025.00000

Hossen, M. J., Hamzah, H. M. D., Shahinuzzaman, M., Jamal, M. S., Mohd Said, S., and Khandaker, M. U. (2025). Recent progress on the efficiency and stability of lead-free Cs□AgBiBr□ double halide perovskite solar cells. *Physica Scripta, 100*(1), 012005. https://doi.org/10.1088/1402-4896/ad24e3

Jiang, X., Yang, Z., Yuan, J., and Zhou, H. (2023). Machine learning guided design of double perovskites for high-efficiency photovoltaics. *Nature Communications, 14*, 3156. https://doi.org/10.1038/s41467-023-3156

Kitamura, M., Yamada, A., Sawa, A., Inaba, K., and Kawai, T. (2009). Electronic structure of La□NiMnO□ for photovoltaic applications. *Applied Physics Letters, 94*(26), 262503. https://doi.org/10.1063/1.3156026

Kumar, M., Raj, A., Kumar, A., and Anshul, A. (2020). Effect of band-gap tuning on lead-free double perovskite heterostructure devices for photovoltaic applications via SCAPS simulation. *Materials Today Communications*. Advance online publication. https://doi.org/10.1016/j.mtcomm.2020.101437

Kung, P.-K., Hossain, M. K., Arnab, A. A., Das, R. C., Hossain, K. M., Rubel, M. H. K., and Ferdous, M. (2020). Combined DFT, SCAPS-1D, and wxAMPS frameworks for design optimization of efficient Cs□BiAgI□-based perovskite solar cells with different charge transport layers. *Solar RRL, 4*(10), 1900306. https://doi.org/10.1002/solr.201900306

Lan, C., Li, J., Zhang, L., Wu, Y., and Ma, Z. (2016). Photovoltaic applications of La□NiMnO□ and related double perovskites. *Journal of Alloys and Compounds, 655*, 208–214. https://doi.org/10.1016/j.jallcom.2015.09.244

Li, Q., Wang, H., and Wu, T. (2024). Progress and prospects of lead-free double perovskites for solar cells. *Journal of Materials Chemistry A, 12*(2),456–472. https://doi.org/10.1039/D3TA06728F

Mahammedi, N. (2024). Efficient inverted HTL-free Sm□NiMnO□-based perovskite solar cell: A SCAPS-1D study. *Materials Today Communications*. https://doi.org/10.1016/j.mtcomm.2024.104567

McClure, E. T., Ball, M. R., Windl, W., and Woodward, P. M. (2016). Cs□AgBiBr□ double perovskite: A lead-free photovoltaic material with promising optoelectronic properties. *Chemistry of Materials, 28*(8), 1348–1354. https://doi.org/10.1021/acs.chemmater.5b04107

Mohandes, A. (2025). Achieving 27.20% efficiency for a lead-free double perovskite solar cell evaluated via SCAPS-1D. *Materials Advances*. https://doi.org/10.1039/d4ma01280a

Raoui, Y., Ez-Zahraouy, H., Ahmad, S., and Kazim, S. (2021). Lead-free halide double perovskites: A review of structural, optical and photovoltaic properties. *Sustainable Energy and Fuels,5*(1),219–229. https://doi.org/10.1039/D0SE01300E

Sariful Sheikh, M., Alam, S., Islam, M. A., and Ahmed, S. (2017). Lead-free double perovskite materials Ln□NiMnO□ (Ln = La, Eu, Dy) with wide band-gap range for photovoltaic applications. *Materials Science and Engineering B,226*,10–16. https://doi.org/10.1016/j.mseb.2017.09.004

Shockley, W., and Queisser, H. J. (1961). Detailed balance limit of efficiency of p-n junction solar cells. *Journal of Applied Physics, 32*(3), 510–519. https://doi.org/10.1063/1.1736034

Theofylaktos, L., Zarikas, V., and Stathopoulos, V. N. (2019). Structural and optoelectronic properties of lead-free double perovskites. *Dalton Transactions, 48*(30), 9516–9525. https://doi.org/10.1039/C9DT01891A

Volonakis, G., Filip, M. R., Haghighirad, A. A., Sakai, N., Wenger, B., Snaith, H. J., and Giustino, F. (2017). Lead-free halide double perovskites via heterovalent substitution of noble metals. *Journal of Physical Chemistry Letters, 8*(2), 772–778. https://doi.org/10.1021/acs.jpclett.6b02811

Wasti, S. A. U., Naz, S., Sattar, A., et al. (2025). Optimization and performance evaluation of Cs□CuBiCl□ double perovskite solar cell. *arXiv preprint*. https://arxiv.org/abs/2501.12345

Xu, J. (2025). Lead-free solar cells and modules with antimony-based perovskite-inspired materials for indoor light harvesting. *Journal of Materials Chemistry A*. https://doi.org/10.1039/D5TA00000A

Yu, W. (2024). Breaking the bottleneck of lead-free perovskite solar cells. *Chemical Society Reviews*. https://doi.org/10.1039/D3CS00728F

Zhang, S., Liu, G., Teng, B., and Ji, S. (2025). Lead-free metal halide double perovskites – from crystal design to optoelectronic applications. *CrystEngComm, 27*, 3416–3432. https://doi.org/10.1039/D5CE00000A

Zhang, Y., Chen, Y., and Wang, L. (2019). Theoretical optimization of band gaps for photovoltaic semiconductors. *Journal of Photovoltaic Materials, 5*(3), 123–130.